Magnetotransport in spin-orbit coupled noncentrosymmetric and Weyl metals

Gautham Varma K.,[1] Azaz Ahmad,[1] Sumanta Tewari,[2] and Gargee Sharma[1]
[1]*School of Physical Sciences, Indian Institute of Technology Mandi, Mandi 175005, India*
[2]*Department of Physics and Astronomy, Clemson University, Clemson, South Carolina 29631, USA*

(Received 21 November 2023; revised 12 February 2024; accepted 22 March 2024; published 3 April 2024)

Recently, chiral anomaly (CA) has been proposed to occur in spin-orbit coupled noncentrosymmetric metals (SOC-NCMs), motivating CA to be a Fermi surface property rather than a Weyl node property. Although the nature of the anomaly is similar in both SOC-NCMs and Weyl systems, here we point out significant fundamental differences between the two. We show that the different nature of the orbital magnetic moment (OMM) in the two systems leads to nontrivial consequences—particularly the sign of the longitudinal magnetoconductance always remains positive in a SOC noncentrosymmetric metal, unlike a Weyl metal that displays either sign. Furthermore, we investigate the planar Hall effect and the geometrical contribution to the Hall effect in the two systems and point out significant differences in the two systems. We conduct our analysis for magnetic and nonmagnetic impurities, making our study important in light of current and upcoming experiments in both SOC-NCMs and Weyl metals.

DOI: 10.1103/PhysRevB.109.165114

I. INTRODUCTION

Chiral anomaly roots its origin in high-energy physics [1,2]. It refers to the nonconservation of left- and right-handed Weyl fermions separately in the presence of external gauge fields. Over the past decade, its unexpected appearance in solid-state systems has caused great excitement in the condensed matter community [3–31]. Specifically, Weyl fermions, discovered as electronic excitations in specific systems [termed as Weyl semimetals (WSMs)], can manifest the anomaly that can be detected via relatively simple transport [10–16] or optical [32–38] measurements. The key requirement is that the elementary excitations should be chiral and relativistic in odd spatial dimensions [39].

The realization of the anomaly has recently been extended to certain other systems distinct from Weyl semimetals [40–50]. Specifically, it has been suggested that the anomaly can be realized in spin-orbit-coupled (SOC) noncentrosymmetric metals (NCMs) that host nonrelativistic fermions with only one relevant band touching point [48]. The effect of the anomaly on charge and thermal transport properties of SOC-NCMs has recently been studied [48,49,51], and it has been suggested that the anomaly results in positive longitudinal magnetoconductance (LMC) [48,49], akin to Weyl semimetals. The sign of LMC has been a subject of much debate and exploration in WSMs. It is expected to crucially depend on the nature of impurities, the strength of the magnetic field, and the strength of the intervalley scattering. Under strong magnetic fields, due to Landau quantization, the LMC sign depends on the nature of scattering impurities [30,52–57].

Recently, we pointed out that the sign of LMC is, in fact, more nuanced [58]. LMC in Weyl systems can typically be expressed as $\sigma_{zz} = \sigma_0 + \sigma_{zz}^{(2)}(B - B_0)^2$. "Strong-sign-reversal" is characterized by the reversal of orientation of the magnetoconductance parabola with respect to the magnetic field, while in "weak-sign-reversal," the magnetoconductivity depends on the direction of the magnetic field and is not correlated with the orientation of the LMC parabola. Figure 1(c) shows a schematic description of strong and weak-sign-reversal of LMC. Specifically, in the case of weak-sign-reversal, LMC is linear in the near zero magnetic field, while the vertex of the parabola (B_0) is shifted from the origin, but the quadratic coefficient of LMC ($\sigma_{zz}^{(2)}$) remains positive. In the case of strong-sign-reversal, importantly, the quadratic coefficient $\sigma_{zz}^{(2)}$ becomes negative. When Landau quantization can be ignored under weak magnetic fields, quasiclassical Boltzmann analysis suggests that sufficiently strong intervalley scattering can reverse the sign of LMC from positive to negative (strong-sign-reversal) [19,20,59]. Whether or not the longitudinal magnetoconductance in SOC-NCMs shows similar characteristics also remains an important and pertinent question in the field. Furthermore, the focus of all the previous works has been particularly on point-like scalar nonmagnetic impurities. The fate of LMC in both spin-orbit-coupled and Weyl metals in the presence of (pseudo)magnetic impurities remains to be determined.

In SOC-NCMs, we focus on the vicinity of one nodal point surrounded by two Fermi surfaces as depicted in Fig. 2(b). This is in contrast to the two separate nodal points and Fermi surfaces we are concerned with in WSMs [Fig. 2(a)]. The role of intranode scattering in WSMs is replaced by intraband scattering in SOC-NCMs. This scattering preserves the chirality of the scattered quasiparticles. Internode scattering in WSMs is equivalent to interband scattering in SOC-NCMs, reversing the quasiparticle chirality. Internode scattering in WSMs requires the transfer of large momentum of the order of separation between the Weyl nodes, which is usually weaker than intranode scattering requiring a small momentum transfer. In contrast, in SOC-NCMs, the momentum transfer with interband scattering is not necessarily small, as both the Fermi surfaces surround a single nodal point. Thus, interband

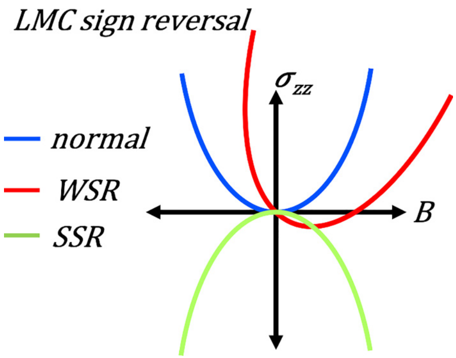

FIG. 1. Schematic figure representing weak-sign-reversal (WSR) and strong-sign-reversal (SSR) compared to normal LMC in Weyl systems.

scattering is expected to be at least as significant in SOC-NCMs as it is in WSMs, and its exploration remains an open question.

In this work, we probe the role of interband scattering in SOC-WSMs and show that in the quasiclassical low-field regime, unlike WSMs, the sign of LMC is *not* sensitive to the relative strength of the interband scattering. Longitudinal magnetoconductance in SOC-NCMs is found to be always positive, irrespective of the strength of the interband scattering. We trace the reason to the orbital magnetic moment (OMM) in SOC-NCMs that is of equal magnitude and sign at both the bands, as compared to the case of WSMs where OMM has equal magnitudes but opposite signs at the two nodes (see Fig. 2). We examine how the subtle difference in OMM can lead to drastic differences in other transport properties, such as the planar Hall conductivity, and also give rise to a finite geometrical contribution to the Hall conductivity in SOC-NCMs. Furthermore, we also analyze all the properties of both WSMs and SOC-NCMs in the presence of both point-like scalar and magnetic impurities, which has remained an open problem so far.

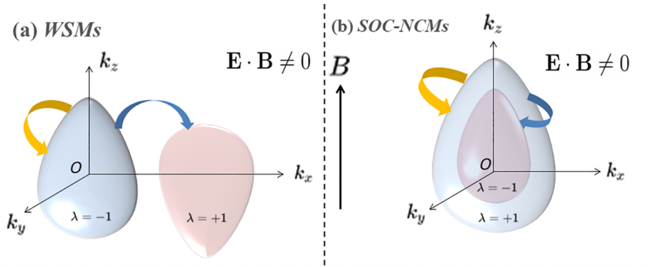

λ	-1	$+1$	-1	$+1$
$\mathbf{\Omega}^\lambda(k)$	$+\frac{\mathbf{k}}{2k^3}$	$-\frac{\mathbf{k}}{2k^3}$	$+\frac{\mathbf{k}}{2k^3}$	$-\frac{\mathbf{k}}{2k^3}$
$\mathbf{m}^\lambda(k)$	$+\frac{ev_F}{2}\frac{\mathbf{k}}{k^2}$	$-\frac{ev_F}{2}\frac{\mathbf{k}}{k^2}$	$-\frac{e\vartheta}{2}\frac{\mathbf{k}}{k^2}$	$-\frac{e\vartheta}{2}\frac{\mathbf{k}}{k^2}$

FIG. 2. Quasiparticle scattering in (a) WSMs and (b) SOC-NCMs. Unlike WSMs, quasiparticle scattering in SOC-NCMs occurs between the surfaces (FSs) associated with a single nodal point. The two Fermi FSs in SOC-NCMs have opposite Berry curvature [$\mathbf{\Omega}^\lambda(\mathbf{k})$], but crucially, unlike WSMs, have the same orbital magnetic moment [$\mathbf{m}^\lambda(\mathbf{k})$]. Blue and yellow arrows represent the internode (interband for SOC-NCMs) and intranode (intraband for SOC-NCMs) scattering, respectively, in WSMs. Here, λ is the band/node index. The oval shape of the Fermi surfaces is due to the coupling of the orbital magnetic moment in an external magnetic field.

II. MODEL AND FORMALISM

We begin with the following extended model of a spin-orbit coupled noncentrosymmetric metal that can be expressed near the high-symmetry point as:

$$H_{\text{soc}}(\mathbf{k}) = \frac{\hbar^2 k^2}{2m}\sigma_0 + \hbar\vartheta\mathbf{k}\cdot\sigma + \hbar\vartheta(k_x t_x + k_z t_z)\sigma_0. \tag{1}$$

Here, m is the effective electron mass. The second term represents the spin-orbit coupling term, and σ denotes the vector of Pauli matrices in the spin space. The third term in the Hamiltonian tilts the dispersion along a particular direction, and the dimensionless parameters t_x and t_z represent the tilting along x- and z-directions, respectively. Similar to the case of WSMs, the tilt term may arise naturally in the bandstructure in SOC-NCMs or may model the effect of strain in the material.

To compare our results with WSM, we use the following prototype model of a two-node time-reversal symmetry broken WSM

$$H_{\text{wsm}} = \left(\sum_{\chi=\pm 1}\hbar v_F\chi\mathbf{k}\cdot\boldsymbol{\sigma}\right) + \hbar v_F(k_x t_x + k_z t_z)\sigma_0. \tag{2}$$

Here, χ is the chirality and v_F is the Fermi velocity. The Hamiltonian in Eq. (1) has the following energy dispersion:

$$\epsilon^\lambda(\mathbf{k}) = \frac{\hbar^2 k^2}{2m} + \lambda\hbar\vartheta k + \hbar\vartheta(k_x t_x + k_z t_z). \tag{3}$$

Here, $\lambda = \mp 1$ is the band index. The corresponding eigenvectors are $|u^\lambda\rangle^T = [\lambda e^{-i\phi}\cos(\theta/2), \sin(\theta/2)]$. We assume that the Fermi energy ϵ_F lies above the nodal point $\mathbf{k} = 0$, and thus we have two Fermi surfaces corresponding to the two energy bands as shown in Fig. 2(b). The Berry curvature ($\mathbf{\Omega}^\lambda_{\mathbf{k}}$) for both these surfaces has equal magnitudes and opposite signs, just like the Fermi surfaces in the vicinity of two nodal points in WSMs. Interestingly, the orbital magnetic moment ($\mathbf{m}^\lambda_{\mathbf{k}}$) carries the same sign and magnitude, distinct from WSMs where the signs are reversed. In the presence of an external magnetic field ($\mathbf{B}$), the orbital magnetic moment couples to the dispersion as $-\mathbf{m}^\lambda_{\mathbf{k}}\cdot\mathbf{B}$ leading to the oval-shaped Fermi surfaces as shown in Fig. 2(b). In WSMs, the coupling is opposite, and thus, the shapes of the surfaces are reversed. The Berry curvature and orbital magnetic moment are given by the following relations:

$$\mathbf{\Omega}^\chi_{\mathbf{k}} = i\nabla_{\mathbf{k}} \times \langle u^\chi(\mathbf{k})|\nabla_{\mathbf{k}}|u^\chi(\mathbf{k})\rangle, \tag{4}$$

$$\mathbf{m}^\chi_{\mathbf{k}} = \frac{-ie}{2\hbar}\text{Im}\left\langle\frac{\partial u^\chi}{\partial\mathbf{k}}\right| \times [\epsilon_0(\mathbf{k}) - \hat{H}^\chi(\mathbf{k})]\left|\frac{\partial u^\chi}{\partial\mathbf{k}}\right\rangle. \tag{5}$$

We study charge transport in the presence of perturbative electric and magnetic fields using the quasiclassical Boltzmann formalism. This is valid in the limits of weak magnetic fields, $B \ll B_c$, where $eB_c\hbar/2m\epsilon_F = 1$. The nonequilibrium

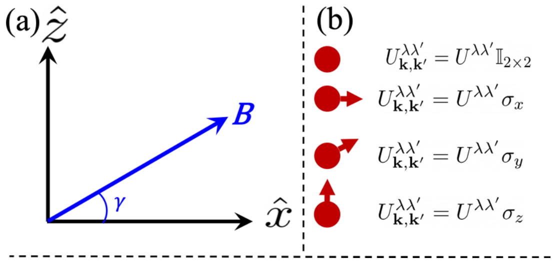

FIG. 3. (a) Orientation of magnetic field in the xz plane. (b) Symbolic interpretation for the types of impurity studied in this article [Eq. (8)].

distribution function $f^\lambda_{\mathbf{k}}$ obeys the following steady-state equation:

$$\dot{\mathbf{r}}^\lambda_{\mathbf{k}} \cdot \nabla_{\mathbf{r}} f^\lambda_{\mathbf{k}} + \dot{\mathbf{k}}^\lambda \cdot \nabla_{\mathbf{k}} f^\lambda_{\mathbf{k}} = I_{\mathrm{coll}}\big[f^\lambda_{\mathbf{k}}\big]. \tag{6}$$

Here, $f^\lambda_{\mathbf{k}} = f_0 + g^\lambda_{\mathbf{k}}$, with f_0 being the Fermi-Dirac distribution and $g^\lambda_{\mathbf{k}}$ is the deviation due to the presence of the external fields. We restrict ourselves to the first order in the electric field, i.e., $g^\lambda_{\mathbf{k}} = -e(\frac{\partial f_0}{\partial \mu})_{\epsilon_F}\mathbf{E}\cdot\mathbf{\Lambda}^\lambda_{\mathbf{k}}$. The collision integral (I_{coll}) in Eq. (6) is chosen in such a way that it can incorporate both interband and intraband scattering, given by

$$I_{\mathrm{coll}}\big[f^\lambda_{\mathbf{k}}\big] = \sum_{\lambda'}\sum_{\mathbf{k}'} \mathbf{W}^{\lambda\lambda'}_{\mathbf{k}\mathbf{k}'}\big(f^{\lambda'}_{\mathbf{k}'} - f^\lambda_{\mathbf{k}}\big), \tag{7}$$

where the scattering rate $\mathbf{W}^{\lambda\lambda'}_{\mathbf{k}\mathbf{k}'}$ calculated using the Fermi's golden rule

$$\mathbf{W}^{\lambda\lambda'}_{\mathbf{k}\mathbf{k}'} = \frac{2\pi n}{\mathcal{V}}\big|\langle u^{\lambda'}(\mathbf{k}')|\,U^{\lambda\lambda'}_{\mathbf{k}\mathbf{k}'}\,|u^\lambda(\mathbf{k})\rangle\big|^2\delta\big(\epsilon^{\lambda'}_{\mathbf{k}'} - \epsilon_F\big). \tag{8}$$

Here, "n" is the impurity concentration, "$\mathcal{V}$" is the system volume, $|u^\lambda(\mathbf{k})\rangle$ is the spinor wave function, $U^{\lambda\lambda'}_{\mathbf{k}\mathbf{k}'}$ is the scattering potential profile, and ϵ_F is the Fermi energy. Here we choose $U^{\lambda\lambda'}_{\mathbf{k}\mathbf{k}'}$ in such a manner that it can include both magnetic and nonmagnetic point-like scattering centers. In general $U^{\lambda\lambda'}_{\mathbf{k}\mathbf{k}'} = U^{\lambda\lambda'}\sigma_i$ with $i = 0, 1, 2, 3$, where $U^{\lambda\lambda'}$ distinguishes the interband ($\lambda \neq \lambda'$) and intraband ($\lambda = \lambda'$) scattering. Here, we work in the geometry represented in Fig. 3(a), i.e., we fix the direction of the electric field along the z direction and rotate the magnetic field in the xz plane that makes an angle γ with respect to the x axis. Further calculation details for the solution of the distribution function $f^\lambda_{\mathbf{k}}$ are presented in the Appendix. Finally, the current is evaluated as $\mathbf{j} = -e\sum_\chi\sum_{\mathbf{k}}\dot{\mathbf{r}}^\chi f^\chi_{\mathbf{k}}$, and the conductance tensor $\hat{\sigma}$ is given by $j_\alpha = \sigma_{\alpha\beta}E_\beta$. Unless otherwise specified, we choose the following values for our calculations: $m = 10^{-32}$ kg, $\vartheta = 5\times10^5\,\mathrm{ms}^{-1}$, $v_F = 10^6\,\mathrm{ms}^{-1}$, $\epsilon_F = 50\,\mathrm{meV}$.

For comparison with an inversion asymmetric WSM (IWSM), we use the following minimum model Hamiltonian that consists of four nodes:

$$H = \sum_{n=1}^{4}\chi_n\hbar v_F\mathbf{k}\cdot\sigma + \hbar v_F t^n_z k_z\sigma_0. \tag{9}$$

Here, χ_n denotes the chirality of the nth node and t^n_z denotes the corresponding tilt parameter. To break inversion symmetry, we chose the tilt configuration as $(1, t_z) = (\chi_1, t^1_z) = (-\chi_2, t^2_z) = (\chi_3, -t^3_z) = (-\chi_4, -t^4_z)$.

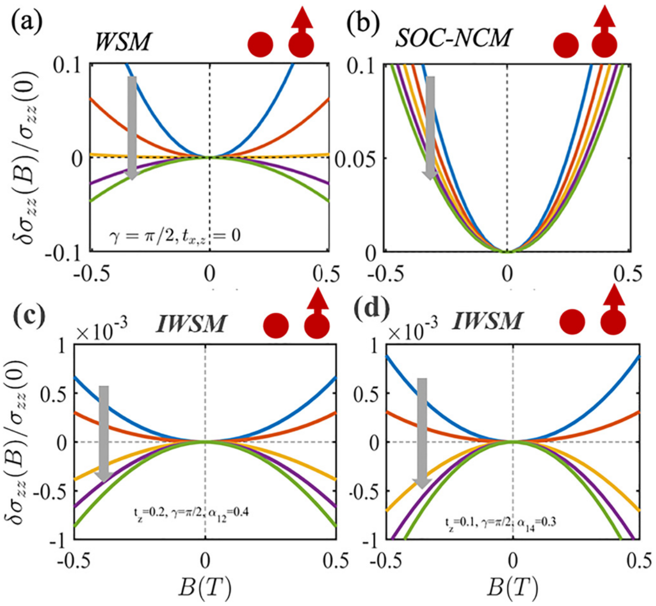

FIG. 4. LMC in Weyl semimetals and SOC-NCMs as a function of the magnetic field for different values of the relative interband (internode for WSMs) scattering strengths α. As we move in the direction of the arrow from the blue to the green curve, α is increased from 0.35 to 1.25. We obtain the same behavior for a nonmagnetic impurity profile, i.e., $U^{\lambda\lambda'}_{\mathbf{k},\mathbf{k}'} = U^{\lambda\lambda'}\sigma_0$, as well as magnetic impurity, i.e, $U^{\lambda\lambda'}_{\mathbf{k},\mathbf{k}'} = U^{\lambda\lambda'}\sigma_z$. (a) For WSM there is strong-sign-reversal above $\alpha > \alpha_c$, (b) For SOC-NCM, there is no sign-reversal for any interband scattering strength. (c) For IWSM, we obtain strong sign reversal for $\alpha_{14} > \alpha_c$ similar to the case for time reversal symmetry broken WSM. (d) A gain, for IWSM, we obtain strong sign reversal for $\alpha_{12} > \alpha_c$.

III. RESULTS

A. Longitudinal magnetoconductance

We first discuss longitudinal magnetoconductance for SOC-NCM and compare it with a standard WSM. We examine the behavior of each impurity type (magnetic and nonmagnetic) individually. In Fig. 4(b) we plot the LMC in SOC-NCM as a function of the magnetic field for different values of the relative interband scattering strengths α (the ratio of interband scattering strength to intraband scattetring strength), for nonmagnetic σ_0 impurities. The LMC is always positive for any value of α. This behavior is in striking contrast to WSMs where LMC changes sign (strong sign-reversal [58]) when $\alpha > \alpha_c$ [Fig. 4(a)]. We understand this behavior as follows. Let us denote the Weyl spinor for a state with momentum $\mathbf{k}$ and chirality quantum number ν by $|\psi_{\mathbf{k}}\rangle^\nu$. The Weyl spinors obey the following symmetry: $|\psi_{+\mathbf{k}}\rangle^+ = |\psi_{-\mathbf{k}}\rangle^-$ and $|\psi_{-\mathbf{k}}\rangle^+ = |\psi_{+\mathbf{k}}\rangle^-$. Within a valley, backscattering of an electron implies $|\psi_{+\mathbf{k}}\rangle^\nu \to |\psi_{-\mathbf{k}}\rangle^\nu$. Since $|\psi_{-\mathbf{k}}\rangle^\nu$ is identical to $|\psi_{+\mathbf{k}}\rangle^{-\nu}$, internode scattering evades backscattering, while intranode scattering does not. Furthermore, the quasiclassical velocity $\dot{\mathbf{r}}^\nu \propto (\mathbf{B}\cdot\mathbf{\Omega}^\nu_{\mathbf{k}})$ [28]. Since $\mathbf{\Omega}^\nu_{\mathbf{k}} = -\chi\hat{\mathbf{k}}/k^2$, this contribution is identical for $|\psi_{+\mathbf{k}}\rangle^\nu$ and $|\psi_{-\mathbf{k}}\rangle^{-\nu}$. Therefore, internode scattering, associated with chiral anomaly can result in negative longitudinal magnetoresistance unlike intranode scattering that always increases resistance [60]. Now, in

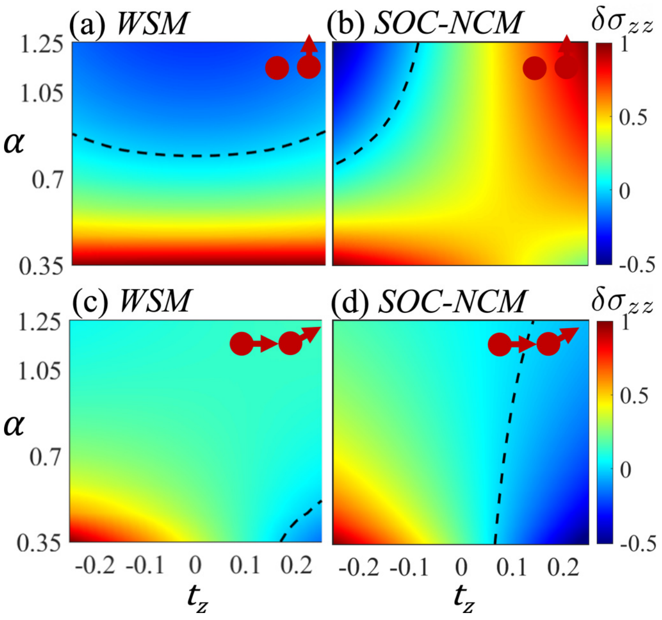

FIG. 5. LMC in Weyl semimetals and SOC-NCMs as a function of the relative interband (internode for WSMs) scattering strengths α and the parameter t_z. The dashed black line shows the contour separating positive and negative LMC regions.

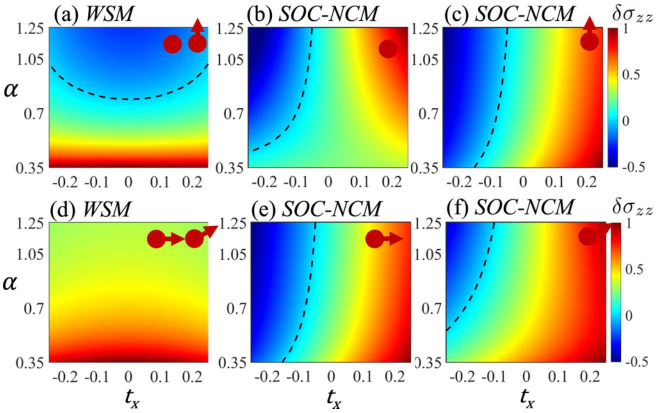

FIG. 6. LMC in WSMs and SOC-NCMs in the presence of t_x parameter. The dashed black line shows the contour separating positive and negative LMC regions.

WSMs, the sign of the OMM is different at Fermi surfaces at both nodes. This breaks the symmetry between them, thus also breaking the symmetry between the chiral partners $|\psi_{\mathbf{k}}\rangle^{\nu}$ and $|\psi_{-\mathbf{k}}\rangle^{-\nu}$. This has been attributed to result in a strong-sign-reversal of LMC [19,20,58]. On the other hand, OMM shifts the energy dispersion in SOC-NCMs in both the Fermi surfaces by the same amount as shown in Fig. 2(b). The symmetry between the chiral partners between both the Fermi surfaces thus remains intact and therefore no sign-reversal is observed.

Since the magnetic-σ_z impurity does not flip the chirality of the quasiparticles in both SOC-NCMs and WSMs, we observe the same effect on LMC as a nonmagnetic impurity (σ_0). The σ_x and σ_y impurities, on the other hand, flip the chirality of the quasiparticles. We obtain quadratic and positive LMC for both WSMs and SOC-NCMs for σ_x and σ_y impurities (not plotted explicitly). It is also possible to have a fair comparison of magnetotransport with an inversion asymmetric WSM (IWSM) as well. The LMC profile of IWSM, as shown in Figs. 4(c) and 4(d), also shows strong sign reversal for sufficiently strong values of intervalley scattering. Note that due to the presence of multiple nodes, multiple internode scatterings are possible. We denote the scattering strength from node 1 to node 2 and node 3 to node 4 by α_{12}, and the scattering strength from node 1 to node 4 and node 2 to node 3 by α_{14}.

Next, we examine LMC as a function of the parameter t_z and α for σ_0 and σ_z impurities in Fig. 5. Here $\delta_{\sigma zz}$ is the normalized change in the magnetoconductance evaluated at some small finite positive magnetic field. We obtain strikingly different behavior for WSMs and SOC-NCMs. For WSMs, the zero-LMC contour $\alpha_c(t_z)$, which separates positive and negative LMC, is now a function of t_z [Fig. 5(a)]. This change of sign corresponds to strong-sign-reversal. For SOC-NCMs, the zero-LMC contour appears for nonzero values of t_z and this change of sign is associated with weak-sign-reversal [Fig. 5(b)]. Specifically, the t_z-term tilts the parabola along a particular direction but does not flip its orientation. We understand the general behavior due to tilt as follows. Tilting the Weyl cones makes the Fermi velocity (and the Fermi momentum) anisotropic across the Fermi surface. For example, when $t_z \neq 0$, $k_F(\theta) = \epsilon_F/(1 + t_z \cos\theta)$. Note that, in general, the Fermi contour depends on the magnitude as well as the sign of the tilt parameter. Flipping the sign of the tilt parameter amounts to switching left movers into right movers and vice versa. Furthermore, the quasiclassical velocity has an additional contribution from the Berry curvature: $\dot{\mathbf{r}}^{\nu} \propto (\mathbf{B} \cdot \mathbf{\Omega}^{\nu}_{\mathbf{k}})$ [28]; its contribution is dependent on the sign of the magnetic field. Due to tilt-induced asymmetry in the Fermi surface, its contribution is also different for left and right movers. This interplay between tilt, anomalous velocity, and the direction of the B field results in the behavior obtained in Fig. 5. In WSMs, the different signs of the orbital magnetic moment associated with the two nodes induce further asymmetry.

In Figs. 5(c) and 5(d) we examine the behavior of LMC as a function of α and t_z for σ_x and σ_y magnetic impurities. In WSMs, we observe weak-sign-reversal for large values of the tilt parameter t_z, and no sign-reversal for smaller values of t_z. Furthermore, increasing internode scattering restores positive LMC. This is in sharp contrast to the effect of σ_0 and σ_z impurities in WSMs, where we observe strong-sign-reversal and decreasing internode scattering restoring positive LMC. In SOC-NCMs, for σ_x and σ_y impurities, the effect of weak-sign-reversal is more pronounced as shown in Fig. 5(d). Again, larger interband scattering restores positive LMC. This feature is understood as follows. The σ_x (or σ_y) impurities flip the chirality of the fermions; further imposing interband scattering back-flips the reversed chirality, and thus interband σ_x scattering behaves like intraband scattering.

In Fig. 6 we compare the behavior of LMC of WSM with that of SOC-NCM in the presence of the tilt parameter t_x. In WSM, just like the case when $t_z \neq 0$, we find that the behavior in the presence of nonmagnetic and σ_z impurities is similar; we observe strong-sign-reversal. The zero-LMC

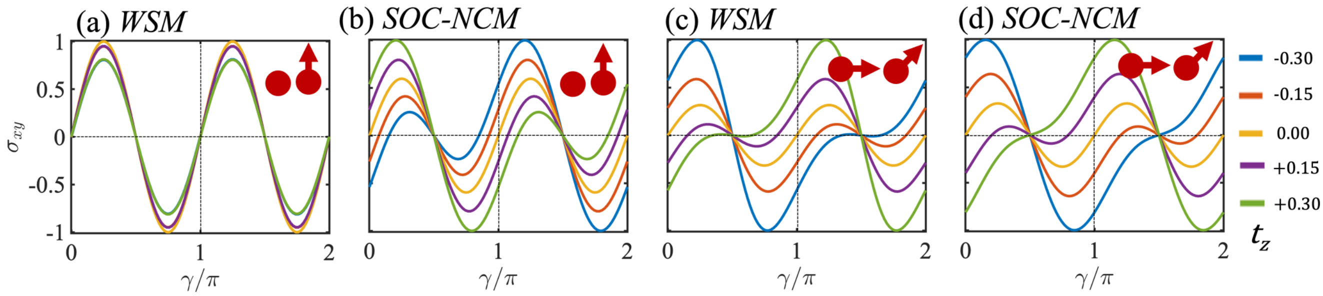

FIG. 7. Planar Hall conductivity for WSM and SOC-NCM for different impurity types in the presence of parameter t_z. Plots are appropriately normalized.

contour $\alpha_c(t_x)$ is qualitatively similar to the case of nonzero t_z, but nevertheless exhibits quantitative differences. In SOC-NCM, weak-sign-reversal is observed. Unlike the $t_z \neq 0$ case, we observe quantitative differences between nonmagnetic and σ_z impurities [Figs. 6(b) and 6(c)]. Surprisingly, WSMs in the presence of σ_x or σ_y impurities, exhibit neither weak-sign-reversal nor strong-sign-reversal in the presence of t_x parameter [Fig. 6(d)]. This can be again understood from the fact that either of these impurity types changes the roles of internode scattering and that tilting the Weyl cone in a direction orthogonal to the direction of the magnetic field does not add an overall linear component to the magnetoconductivity. For SOC-NCM, we observe weak-sign-reversal, with quantitative differences between σ_x and σ_y impurities.

Before closing this subsection, we discuss how the interband scattering strength can be tuned. Intraband scattering involves a small momentum transfer while interband scattering involves a relatively large momentum transfer. Since the radial separation of the bands in momentum space is larger for higher values of spin-orbit coupling parameter ϑ, interband scattering is expected to be suppressed in materials that have large ϑ. Furthermore, since the Zeeman field also spin-splits the bands causing an increase in the radial separation of the two Fermi surfaces, this can also lead to reduced interband scattering. Finally, the type of impurities (scalar or charged) also affects the momentum transfer during electron-impurity scattering. Therefore tuning the scattering ratio would require tuning the strength of the magnetic field and/or doping the sample with different impurities.

B. Planar Hall conductance

We next discuss the planar Hall conductance in SOC-NCM and compare the results with a standard WSM. In WSMs, the PHC can be expressed as [58]

$$\sigma_{xz}(B) = \sigma_{xz}^{(2)}(B-B_0)^2 + \sigma_{xz}^{(0)}, \tag{10}$$

where B_0 is the vertex of the parabola and $\sigma_{xz}^{(2)}$ is the quadratic coefficient. The above form allows us to generalize PHC away from the origin, i.e., $B_0 \neq 0$. The angular dependence for WSM is $\sin(2\gamma)$ for a point-like nonmagnetic impurity profile. We find that this dependence is retained for magnetic impurities pointing in the z direction as well [Fig. 7(a)], and tilting the Weyl cones ($t_z \neq 0$) only has a quantitative effect. In contrast, SOC-NCMs have a qualitatively different dependence on t_z [Fig. 7(b)]. We observe that unlike in WSMs, the planar Hall conductance in SOC-NCMs exhibits weak-sign-reversal as a function of the parameter t_z. For σ_x and σ_y impurities, PHC in both WSMs and SOC-NCMs exhibit weak-sign-reversal and exhibit similar qualitative behavior [Figs. 7(c) and 7(d)]. In both systems, interband (internode) scattering is found to have no significant qualitative effect on planar Hall conductance.

For the nodes tilted along the x direction, we observe qualitatively very different behavior. For σ_0 point-like impurities, the $\sin 2\gamma$ trend is observed irrespective of the value of t_x, as expected for Weyl cones that are oriented in the same direction. We find qualitatively similar behavior irrespective of the impurity type [Fig. 8(a)]. Note that if the Weyl cones were oriented opposite to each other, one instead finds a $\sin\gamma$ behavior of PHC [16]. In the case of SOC-NCMs, one finds a transition from $\sin 2\gamma$ trend to $\sin\gamma$ as the parameter t_x is increased from zero in either direction (Fig. 8). Like WSMs, we observe qualitatively similar behavior for both magnetic (any direction) and nonmagnetic impurities.

C. Anomalous contribution to the Hall Conductance

In WSMs, the nonvanishing anomalous Hall conductance (AHC) has been attributed to the presence of a finite vector $\mathbf{k}_0$ that separates Weyl cones of opposite chiralities. The net AHC is given by $\sigma_{xy}^{a} = e^2 k_0/\hbar$. In the presence of time-reversal symmetry, multiple such vectors add up to zero, and AHC is zero. It is noteworthy that the intrinsic AHC contribution of one node, which is given by the integral of the Berry curvature of the filled band up to the Fermi surface, exactly cancels the contribution of the other node. The nonzero AHC in TR-broken WSMs is understood by considering a gapped

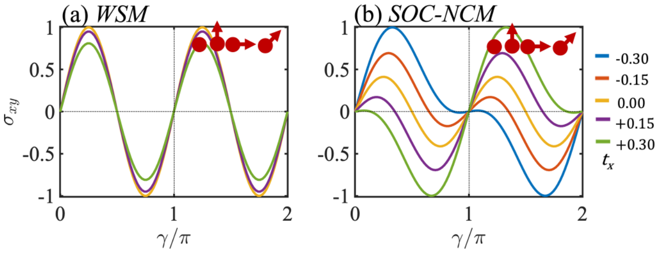

FIG. 8. Planar Hall conductivity for WSM and SOC-NCM for different impurity types in the presence of parameter t_x. Plots are appropriately normalized.

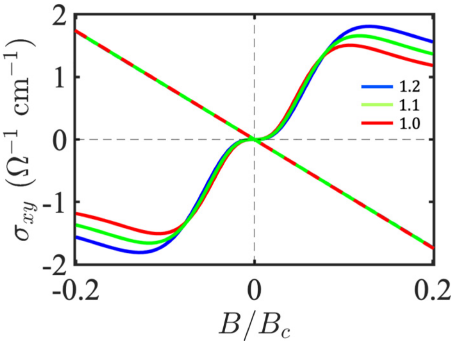

FIG. 9. Geometrical contribution to the Hall conductivity showing a nonmonotonic behavior. The legends indicate the strength of spin-orbit coupling parameter ϑ in units of $10^5\,\mathrm{ms}^{-1}$. We chose $g = 2$. The dashed lines show the normal Hall response.

two-dimensional (2D) Chern insulator $H(\mathbf{k}_\perp, k_z)$ that undergoes a topological phase transition at the Weyl node [7].

In SOC-NCMs, we particularly focus on a single nodal point. It is expected that the two Fermi surfaces that enclose the nodal point cancel out their contributions of anomalous Hall conductivity, but as we will show next, the presence of an external magnetic field induces finite anomalous contribution to the Hall conductivity. In the presence of an external magnetic field, Zeeman coupling will introduce an additional term in the Hamiltonian given by [61–63]

$$H_z = -g\mu_B \boldsymbol{\sigma} \cdot \mathbf{B}. \tag{11}$$

This causes an opposite energy shift in both bands. Furthermore, the anomalous shift in the energy dispersion due to the orbital magnetic moment ($\epsilon^\lambda_\mathbf{k} \rightarrow \epsilon^\lambda_\mathbf{k} - \mathbf{m}^\lambda_\mathbf{k} \cdot \mathbf{B}$). Both of these effects, in concurrence, lead to a finite and measurable anomalous contribution to the Hall conductance, which at zero temperature is calculated as

$$\sigma^a_{xy} = \frac{e^2}{\hbar} \sum_{\lambda=\pm 1} \int \frac{d^3\mathbf{k}}{(2\pi)^3} \mathcal{D}^\lambda_\mathbf{k} \theta\big(\epsilon_F - \epsilon^\lambda_\mathbf{k}\big) \Omega^\lambda_z(\mathbf{k}), \tag{12}$$

where $\mathcal{D}^\lambda_\mathbf{k} = (1 + e\mathbf{B} \cdot \boldsymbol{\Omega}^\lambda_\mathbf{k}/\hbar)$. In Fig. 9 we plot the geometrical contribution to the Hall conductivity for SOC-NCM as evaluated from Eq. (12). Interestingly, the behavior is nonmonotonic with respect to the magnetic field, and for low-enough magnetic field, the anomalous contribution is found to be independent of the strength of the spin-orbit coupling parameter. The nonmonotonicity can be understood as follows. With an increasing magnitude of the magnetic field, the net Berry curvature contribution increases, but eventually decreases for larger magnetic fields as the magnitude of the Berry curvature itself reduces. This can be easily tested in current and upcoming transport experiments in SOC-NCMs. We may also compare the magnitude of the anomalous contribution to the normal Hall contribution driven by Lorentz force. The normal Hall contribution is given by

$$\sigma_{xy} = -\frac{e^3\tau^2 B}{\hbar^2} \int \frac{d^3\mathbf{k}}{(2\pi)^3} \left(\frac{-\partial f_0}{\partial \epsilon_\mathbf{k}}\right) \left(\frac{v_x^2 \partial^2 \epsilon_\mathbf{k}}{\partial k_y^2} - \frac{v_x v_y \partial^2 \epsilon_\mathbf{k}}{\partial k_x \partial k_y}\right). \tag{13}$$

It is important to note that the magnitude of the normal Hall effect depends crucially on the scattering time τ. In Fig. 9, we also plot the normal Hall response for a typical value of $\tau \sim 10^{-12}$s. We may expect a much lesser (higher) normal Hall response for disordered (cleaner) samples. Before closing this section, we briefly comment on the prospect of observing a similar effect in time-reversal symmetric WSMs. A TR-symmetric WSM must have at least four Weyl nodes. The orbital magnetic moment will shift the energy bands with positive chirality and negative chirality by equal amounts but differing in their overall sign. Therefore a net nonzero contribution from the Berry curvature is expected that will give rise to the anomalous contribution in the Hall conductivity. A similar nonmonotonicity maybe expected as well.

IV. CONCLUSION AND DISCUSSION

Chiral anomaly is a Fermi surface property with similar characteristics in Weyl and spin-orbit coupled noncentrosymmetric metals. It manifests itself in the measurement of longitudinal magnetoconductance and the planar Hall conductance. However, in striking contrast to WSMs, where the sign of the LMC is sensitive to the internode scattering strength, the sign of the LMC in SOC-NCMs is independent of the interband scattering strength and always remains positive. The reason is traced down to the subtle difference in the orbital magnetic moment in WSMs and SOC-NCMs. Orbital magnetic moment in SOC-NCMs is of equal magnitudes and signs in both the bands but has opposite signs at the two nodes in WSMs. This difference also yields drastic differences in other transport properties, such as the planar Hall conductivity. To be more precise, sign-reversal is induced by sufficiently strong intervalley scattering only in conjunction with the chiral energy shift induced by OMM. Since chiral energy shift does not occur in SOC-NCMs in the presence of OMM, we do not see sign-reversal even for very strong interband scattering strengths. Therefore, OMM effect is more crucial for transport properties such as strong-sign-reversal. We also examined all the properties in the presence of a tilt parameter (t_z and t_x) and for different impurity types (magnetic and nonmagnetic). The behavior for σ_0 and σ_z impurities was found to be qualitatively similar to each other as they do not flip with chirality. On the other hand, σ_x and σ_y flip the chirality and behave qualitatively similar to each other. Lastly, we predict that the combination of the anomalous orbital magnetic moment and the Zeeman field gives rise to a geometrical contribution to the Hall conductivity in SOC-NCMs that is nonmonotonic in the magnetic field. Our study is highly pertinent in light of current and upcoming experiments in the field of spin-orbit-coupled noncentrosymmetric and Weyl metals.

ACKNOWLEDGMENTS

G.V.K. and A.A. acknowledge financial support from IIT Mandi HTRA. G.S. acknowledges support from IIT Mandi Seed Grant. We thank Shubhanshu Karoliya for his technical support.

APPENDIX: MAXWELL BOLTZMANN TRANSPORT THEORY

Due to Berry phase effects, in the presence of electric and magnetic fields, the semiclassical dynamics of the Bloch electrons are modified and governed by the following equation [19,28]:

$$\dot{\mathbf{r}}^{\lambda} = \mathcal{D}^{\lambda}\left(\frac{e}{\hbar}(\mathbf{E}\times\mathbf{\Omega}^{\lambda}) + \frac{e}{\hbar}(\mathbf{v}^{\lambda}\cdot\mathbf{\Omega}^{\lambda})\mathbf{B} + \mathbf{v}_{\mathbf{k}}^{\lambda}\right),$$

$$\dot{\mathbf{p}}^{\lambda} = -e\mathcal{D}^{\lambda}\left(\mathbf{E} + \mathbf{v}_{\mathbf{k}}^{\lambda}\times\mathbf{B} + \frac{e}{\hbar}(\mathbf{E}\cdot\mathbf{B})\mathbf{\Omega}^{\lambda}\right), \tag{A1}$$

where $\mathbf{v}_{\mathbf{k}}^{\lambda} = \frac{1}{\hbar}\frac{\partial\epsilon^{\lambda}(\mathbf{k})}{\partial\mathbf{k}}$ is the band velocity, $\mathbf{\Omega}^{\lambda} = -\lambda\mathbf{k}/2k^3$ is the Berry curvature, and $\mathcal{D}^{\lambda} = (1 + e\mathbf{B}\cdot\mathbf{\Omega}^{\lambda}/\hbar)^{-1}$ is the factor modifying the density of the states in the presence of the Berry curvature. The self-rotation of the Bloch wave packet also gives rise to an orbital magnetic moment, $\mathbf{m}_{\mathbf{k}}^{\lambda}$ [64]. In the presence of a magnetic field, the orbital magnetic moment shifts the energy dispersion as $\epsilon_{\mathbf{k}}^{\lambda} \rightarrow \epsilon_{\mathbf{k}}^{\lambda} - \mathbf{m}_{\mathbf{k}}^{\lambda}\cdot\mathbf{B}$. Using Eqs. (A1) and (7) and retaining terms only up to linear order in electric and magnetic fields, the Boltzmann transport equation becomes

$$\left[\left(\frac{\partial f_0^{\lambda}}{\partial\epsilon_{\mathbf{k}}^{\lambda}}\right)\mathbf{E}\cdot\left(\mathbf{v}_{\mathbf{k}}^{\lambda} + \frac{e\mathbf{B}}{\hbar}(\mathbf{\Omega}^{\lambda}\cdot\mathbf{v}_{\mathbf{k}}^{\lambda})\right)\right] = -\frac{1}{e\mathcal{D}^{\lambda}}\sum_{\lambda'}\sum_{\mathbf{k}'} W_{\mathbf{k}\mathbf{k}'}^{\lambda\lambda'}\left(g_{\mathbf{k}'}^{\lambda} - g_{\mathbf{k}}^{\lambda}\right). \tag{A2}$$

We fixed the direction of the electric field along increasing x-direction, and the magnetic field is rotated in xz-plane (see Fig. 3). Therefore, $\mathbf{E} = E(0, 0, 1)$ and $\mathbf{B} = B(\cos\gamma, 0, \sin\gamma)$. In this case, only the z-component of $\mathbf{\Lambda}$ is relevant. Therefore Eq. (A2) reduces to

$$\mathcal{D}^{\lambda}(k)\left[v_{\mathbf{k}}^{\lambda,z} + \frac{eB\sin\gamma}{\hbar}\left(\mathbf{v}_{\mathbf{k}}^{\lambda}\cdot\mathbf{\Omega}_{k}^{\lambda}\right)\right] = \sum_{\lambda'\mathbf{k}'}\mathbf{W}_{\mathbf{k}\mathbf{k}'}^{\lambda\lambda'}\left(\Lambda_{\mathbf{k}'}^{\lambda'} - \Lambda_{\mathbf{k}}^{\lambda}\right). \tag{A3}$$

We define the valley scattering time ($\tau_{\mathbf{k}}^{\lambda}$) as follows:

$$\frac{1}{\tau_{\mathbf{k}}^{\lambda}(\theta,\phi)} = \sum_{\lambda'}\mathcal{V}\int\frac{d^3\mathbf{k}'}{(2\pi)^3}\left(\mathcal{D}_{\mathbf{k}'}^{\lambda'}\right)^{-1}\mathbf{W}_{\mathbf{k}\mathbf{k}'}^{\lambda\lambda'}. \tag{A4}$$

$\mathbf{W}_{\mathbf{k}\mathbf{k}'}^{\lambda\lambda'}$ is defined in Eq. (8) and the corresponding overlap of the Bloch wave function is $\mathcal{G}_i^{\lambda\lambda'}(\theta,\phi) = [1 + \lambda\lambda'\xi_i(\cos\theta\cos\theta' + \alpha_i\sin\theta\sin\theta'\cos\phi\cos\phi' + \beta_i\sin\theta\sin\theta'\sin\phi\sin\phi']$ with $i = 0, 1, 2, 3$ (see Table I). Taking the Berry phase into account and corresponding change in the density of states, $\sum_k \longrightarrow \mathcal{V}\int\frac{d^3\mathbf{k}}{(2\pi)^3}\mathcal{D}^{\lambda}(k)$, Eq. (A3) becomes

$$h_{\mu}^{\lambda}(\theta,\phi) + \frac{\Lambda_{\mu,i}^{\lambda}(\theta,\phi)}{\tau_{\mu,i}^{\lambda}(\theta,\phi)} = \sum_{\lambda'}\mathcal{V}\int\frac{d^3\mathbf{k}'}{(2\pi)^3}\mathcal{D}^{\lambda'}(k')\mathbf{W}_{\mathbf{k}\mathbf{k}'}^{\lambda\lambda'}\Lambda_{\mu,i}^{\lambda'}(\theta',\phi'). \tag{A5}$$

TABLE I. The signs of α, β, and ξ are used in the expression of overlap of the Bloch wave function [see Eq. (A4)]. $\sigma_{x,y,z}$ are the components of the Pauli spin vector and $\mathbb{I}_{2\times2}$ is the identity matrix.

i	σ_i	α_i	β_i	ξ_i
0	$\mathbb{I}_{2\times2}$	+1	+1	+1
1	σ_x	−1	+1	−1
2	σ_y	+1	−1	−1
3	σ_z	−1	−1	+1

Here $h_{\mu}^{\lambda}(\theta,\phi) = \mathcal{D}^{\lambda_{\mathbf{k}}}[v_{z,\mathbf{k}}^{\lambda} + eB\sin\gamma(\mathbf{\Omega}_k^{\lambda}\cdot\mathbf{v}_{\mathbf{k}}^{\lambda})]$. In the zero-temperature limit, for a constant Fermi energy surface, Eq. (A4) and right-hand side of Eq. (A5) is reduced to the integration over θ' and ϕ':

$$\frac{1}{\tau_{\mu,i}^{\lambda}(\theta,\phi)} = \mathcal{V}\sum_{\lambda'}\Pi^{\lambda\lambda'}\iint\frac{(k')^3\sin\theta'}{\left|\mathbf{v}_{k'}^{\lambda'}\cdot\mathbf{k}'^{\lambda'}\right|}d\theta' d\phi'\mathcal{G}_i^{\lambda\lambda'}\left(D_{\mathbf{k}'}^{\lambda'}\right)^{-1}, \tag{A6}$$

$$\mathcal{V}\sum_{\lambda'}\Pi^{\lambda\lambda'}\iint f^{\lambda'}(\theta',\phi')\mathcal{G}_i^{\lambda\lambda'}d\theta' d\phi' \times \left[d^{\lambda'} - h_{\mu}^{\lambda'}(\theta',\phi') + a^{\lambda'}\cos\theta' + b^{\lambda'}\sin\theta'\cos\phi' + c^{\lambda'}\sin\theta'\cos\phi'\right], \tag{A7}$$

where $\Pi^{\lambda\lambda'} = N|U^{\lambda\lambda'}|^2/4\pi^2\hbar^2$, $f^{\lambda}(\theta,\phi) = \frac{(k)^3}{|\mathbf{v}_{\mathbf{k}}^{\lambda}\cdot\mathbf{k}^{\lambda}|}\sin\theta(\mathcal{D}_{\mathbf{k}}^{\eta})^{-1}$ $\tau_{\mu}^{\lambda}(\theta,\phi)$. Using ansatz $\Lambda_{\mathbf{k}}^{\lambda} = [d^{\lambda} - h_{k'}^{\lambda} + a^{\lambda}\cos\phi + b^{\lambda}\sin\theta\cos\phi + c^{\lambda}\sin\theta\sin\phi]\tau_{\mu}^{\lambda}(\theta,\phi)$ the above equation is written in the following form:

$$d^{\lambda} + a^{\lambda}\cos\phi + b^{\lambda}\sin\theta\cos\phi + c^{\lambda}\sin\theta\sin\phi = \sum_{\lambda'}\mathcal{V}\Pi^{\lambda\lambda'}\iint f^{\lambda'}(\theta',\phi')d\theta' d\phi'\left[d^{\lambda'} - h_{k'}^{\lambda'} + a^{\lambda'}\cos\theta' + b^{\lambda'}\sin\theta'\cos\phi' + c^{\lambda'}\sin\theta'\sin\phi'\right]. \tag{A8}$$

When the aforementioned equation is explicitly put out (for each value of i), it appears as seven simultaneous equations that must be solved for eight variables. The particle number conservation provides another restriction

$$\sum_{\lambda}\sum_{\mathbf{k}} g_{\mathbf{k}}^{\lambda} = 0. \tag{A9}$$

For the eight unknowns $(d^{\pm1}, a^{\pm1}, b^{\pm1}, c^{\pm1})$, Eqs. (A8) and (A9) are simultaneously solved with Eq. (A6). Due to the intricate structure of the equations, all two-dimensional integrals with respect to θ' and ϕ' the simultaneous equations' solution are carried out numerically.

[1] S. L. Adler, Axial-vector vertex in spinor electrodynamics, Phys. Rev. **177**, 2426 (1969).

[2] J. S. Bell and R. Jackiw, A PCAC puzzle: $\pi^0 \to \gamma\gamma$ in the σ-model, Nuov Cim A **60**, 47 (1969).

[3] N. P. Armitage, E. J. Mele, and A. Vishwanath, Weyl and Dirac semimetals in three-dimensional solids, Rev. Mod. Phys. **90**, 015001 (2018).

[4] G. E. Volovik, *The Universe in a Helium Droplet*, Vol. 117 (Oxford University Press, Oxford, 2003).

[5] H. B. Nielsen and M. Ninomiya, No-go theorum for regularizing chiral fermions, Phys. Lett. B **105**, 219 (1981).

[6] H. B. Nielsen and M. Ninomiya, The Adler-Bell-Jackiw anomaly and Weyl fermions in a crystal, Phys. Lett. B **130**, 389 (1983).

[7] X. Wan, A. M. Turner, A. Vishwanath, and S. Y. Savrasov, Topological semimetal and Fermi-arc surface states in the electronic structure of pyrochlore iridates, Phys. Rev. B **83**, 205101 (2011).

[8] G. Xu, H. Weng, Z. Wang, X. Dai, and Z. Fang, Chern semimetal and the quantized anomalous Hall effect in $HgCr_2Se_4$, Phys. Rev. Lett. **107**, 186806 (2011).

[9] A. A. Zyuzin, S. Wu, and A. A. Burkov, Weyl semimetal with broken time reversal and inversion symmetries, Phys. Rev. B **85**, 165110 (2012).

[10] D. T. Son and B. Z. Spivak, Chiral anomaly and classical negative magnetoresistance of Weyl metals, Phys. Rev. B **88**, 104412 (2013).

[11] K.-S. Kim, H.-J. Kim, and M. Sasaki, Boltzmann equation approach to anomalous transport in a Weyl metal, Phys. Rev. B **89**, 195137 (2014).

[12] R. Lundgren, P. Laurell, and G. A. Fiete, Thermoelectric properties of Weyl and Dirac semimetals, Phys. Rev. B **90**, 165115 (2014).

[13] A. Cortijo, Linear magnetochiral effect in Weyl semimetals, Phys. Rev. B **94**, 241105(R) (2016).

[14] G. Sharma, P. Goswami, and S. Tewari, Nernst and magnetothermal conductivity in a lattice model of Weyl fermions, Phys. Rev. B **93**, 035116 (2016).

[15] V. A. Zyuzin, Magnetotransport of Weyl semimetals due to the chiral anomaly, Phys. Rev. B **95**, 245128 (2017).

[16] S. Nandy, G. Sharma, A. Taraphder, and S. Tewari, Chiral anomaly as the origin of the planar Hall effect in Weyl semimetals, Phys. Rev. Lett. **119**, 176804 (2017).

[17] K. Das and A. Agarwal, Berry curvature induced thermopower in type-I and type-II Weyl semimetals, Phys. Rev. B **100**, 085406 (2019).

[18] A. Kundu, Z. B. Siu, H. Yang, and M. B. Jalil, Magnetotransport of Weyl semimetals with tilted Dirac cones, New J. Phys. **22**, 083081 (2020).

[19] A. Knoll, C. Timm, and T. Meng, Negative longitudinal magnetoconductance at weak fields in Weyl semimetals, Phys. Rev. B **101**, 201402(R) (2020).

[20] G. Sharma, S. Nandy, and S. Tewari, Sign of longitudinal magnetoconductivity and the planar Hall effect in Weyl semimetals, Phys. Rev. B **102**, 205107 (2020).

[21] G. Bednik, K. S. Tikhonov, and S. V. Syzranov, Magnetotransport and internodal tunnelling in Weyl semimetals, Phys. Rev. Res. **2**, 023124 (2020).

[22] L. P. He, X. C. Hong, J. K. Dong, J. Pan, Z. Zhang, J. Zhang, and S. Y. Li, Quantum transport evidence for the three-dimensional Dirac semimetal phase in Cd_3As_2, Phys. Rev. Lett. **113**, 246402 (2014).

[23] T. Liang, Q. Gibson, M. N. Ali, M. Liu, R. J. Cava, and N. P. Ong, Ultrahigh mobility and giant magnetoresistance in the Dirac semimetal Cd_3As_2, Nat. Mater. **14**, 280 (2015).

[24] C.-L. Zhang, S.-Y. Xu, I. Belopolski, Z. Yuan, Z. Lin, B. Tong, G. Bian, N. Alidoust, C.-C. Lee, S.-M. Huang *et al.*, Signatures of the Adler–Bell–Jackiw chiral anomaly in a Weyl fermion semimetal, Nat. Commun. **7**, 10735 (2016).

[25] Q. Li, D. E. Kharzeev, C. Zhang, Y. Huang, I. Pletikosić, A. Fedorov, R. Zhong, J. Schneeloch, G. Gu, and T. Valla, Chiral magnetic effect in $ZrTe_5$, Nat. Phys. **12**, 550 (2016).

[26] J. Xiong, S. K. Kushwaha, T. Liang, J. W. Krizan, M. Hirschberger, W. Wang, R. J. Cava, and N. P. Ong, Evidence for the chiral anomaly in the Dirac semimetal Na_3Bi, Science **350**, 413 (2015).

[27] M. Hirschberger, S. Kushwaha, Z. Wang, Q. Gibson, S. Liang, C. A. Belvin, B. A. Bernevig, R. J. Cava, and N. P. Ong, The chiral anomaly and thermopower of Weyl fermions in the half-Heusler GdPtBi, Nat. Mater. **15**, 1161 (2016).

[28] D. T. Son and N. Yamamoto, Berry curvature, triangle anomalies, and the chiral magnetic effect in Fermi liquids, Phys. Rev. Lett. **109**, 181602 (2012).

[29] P. Goswami and S. Tewari, Axionic field theory of $(3+1)$-dimensional Weyl semimetals, Phys. Rev. B **88**, 245107 (2013).

[30] P. Goswami, J. H. Pixley, and S. Das Sarma, Axial anomaly and longitudinal magnetoresistance of a generic three-dimensional metal, Phys. Rev. B **92**, 075205 (2015).

[31] S. Zhong, J. Orenstein, and J. E. Moore, Optical gyrotropy from axion electrodynamics in momentum space, Phys. Rev. Lett. **115**, 117403 (2015).

[32] P. Goswami, G. Sharma, and S. Tewari, Optical activity as a test for dynamic chiral magnetic effect of Weyl semimetals, Phys. Rev. B **92**, 161110(R) (2015).

[33] A. L. Levy, A. B. Sushkov, F. Liu, B. Shen, N. Ni, H. D. Drew, and G. S. Jenkins, Optical evidence of the chiral magnetic anomaly in the Weyl semimetal TaAs, Phys. Rev. B **101**, 125102 (2020).

[34] J.-M. Parent, R. Côté, and I. Garate, Magneto-optical Kerr effect and signature of the chiral anomaly in a Weyl semimetal in magnetic field, Phys. Rev. B **102**, 245126 (2020).

[35] Z. Song, J. Zhao, Z. Fang, and X. Dai, Detecting the chiral magnetic effect by lattice dynamics in Weyl semimetals, Phys. Rev. B **94**, 214306 (2016).

[36] P. Rinkel, P. L. S. Lopes, and I. Garate, Signatures of the chiral anomaly in phonon dynamics, Phys. Rev. Lett. **119**, 107401 (2017).

[37] X. Yuan, C. Zhang, Y. Zhang, Z. Yan, T. Lyu, M. Zhang, Z. Li, C. Song, M. Zhao, P. Leng *et al.*, The discovery of dynamic chiral anomaly in a Weyl semimetal NbAs, Nat. Commun. **11**, 1259 (2020).

[38] B. Cheng, T. Schumann, S. Stemmer, and N. Armitage, Probing charge pumping and relaxation of the chiral anomaly in a Dirac semimetal, Sci. Adv. **7**, eabg0914 (2021).

[39] K. Fujikawa and H. Suzuki, *Path Integrals and Quantum Anomalies* (Oxford University Press, New York, 2004).

[40] Y. Gao, S. A. Yang, and Q. Niu, Intrinsic relative magnetoconductivity of nonmagnetic metals, Phys. Rev. B **95**, 165135 (2017).

[41] X. Dai, Z. Z. Du, and H.-Z. Lu, Negative magnetoresistance without chiral anomaly in topological insulators, Phys. Rev. Lett. **119**, 166601 (2017).

[42] A. V. Andreev and B. Z. Spivak, Longitudinal negative magnetoresistance and magnetotransport phenomena in conventional and topological conductors, Phys. Rev. Lett. **120**, 026601 (2018).

[43] H.-W. Wang, B. Fu, and S.-Q. Shen, Intrinsic magnetoresistance in three-dimensional Dirac materials with low carrier density, Phys. Rev. B **98**, 081202(R) (2018).

[44] S. Nandy, A. Taraphder, and S. Tewari, Berry phase theory of planar Hall effect in topological insulators, Sci. Rep. **8**, 14983 (2018).

[45] B. Fu, H.-W. Wang, and S.-Q. Shen, Quantum magnetotransport in massive Dirac materials, Phys. Rev. B **101**, 125203 (2020).

[46] O. Pal, B. Dey, and T. K. Ghosh, Berry curvature induced magnetotransport in 3D noncentrosymmetric metals, J. Phys.: Condens. Matter **34**, 025702 (2022).

[47] H.-W. Wang, B. Fu, and S.-Q. Shen, Helical symmetry breaking and quantum anomaly in massive Dirac fermions, Phys. Rev. B **104**, L241111 (2021).

[48] S. Cheon, G. Y. Cho, K.-S. Kim, and H.-W. Lee, Chiral anomaly in noncentrosymmetric systems induced by spin-orbit coupling, Phys. Rev. B **105**, L180303 (2022).

[49] S. Das, K. Das, and A. Agarwal, Chiral anomalies in three-dimensional spin-orbit coupled metals: Electrical, thermal, and gravitational anomalies, Phys. Rev. B **108**, 045405 (2023).

[50] B. Sadhukhan and T. Nag, Effect of chirality imbalance on Hall transport of $\mathrm{PrRhC_2}$, Phys. Rev. B **107**, L081110 (2023).

[51] S. Verma, T. Biswas, and T. K. Ghosh, Thermoelectric and optical probes for a Fermi surface topology change in noncentrosymmetric metals, Phys. Rev. B **100**, 045201 (2019).

[52] H.-Z. Lu, S.-B. Zhang, and S.-Q. Shen, High-field magnetoconductivity of topological semimetals with short-range potential, Phys. Rev. B **92**, 045203 (2015).

[53] C.-Z. Chen, H. Liu, H. Jiang, and X. C. Xie, Positive magnetoconductivity of Weyl semimetals in the ultraquantum limit, Phys. Rev. B **93**, 165420 (2016).

[54] S.-B. Zhang, H.-Z. Lu, and S.-Q. Shen, Linear magnetoconductivity in an intrinsic topological Weyl semimetal, New J. Phys. **18**, 053039 (2016).

[55] J. Shao and L. Yan, Magneto-conductivity of tilted type-I Weyl semimetals with different types of impurities, AIP Adv. **9**, 045319 (2019).

[56] X. Li, B. Roy, and S. Das Sarma, Weyl fermions with arbitrary monopoles in magnetic fields: Landau levels, longitudinal magnetotransport, and density-wave ordering, Phys. Rev. B **94**, 195144 (2016).

[57] X.-T. Ji, H.-Z. Lu, Z.-G. Zhu, and G. Su, Effect of the screened coulomb disorder on magneto-transport in Weyl semimetals, J. Appl. Phys. **123**, 203901 (2018).

[58] A. Ahmad, K. V. Raman, S. Tewari, and G. Sharma, Longitudinal magnetoconductance and the planar Hall conductance in inhomogeneous Weyl semimetals, Phys. Rev. B **107**, 144206 (2023).

[59] C. Xiao, H. Chen, Y. Gao, D. Xiao, A. H. MacDonald, and Q. Niu, Linear magnetoresistance induced by intra-scattering semiclassics of Bloch electrons, Phys. Rev. B **101**, 201410(R) (2020).

[60] G. Sharma, S. Nandy, K. V. Raman, and S. Tewari, Revisiting magnetotransport in Weyl semimetals, Phys. Rev. B **107**, 115161 (2023).

[61] G. Sharma, C. Moore, S. Saha, and S. Tewari, Nernst effect in Dirac and inversion-asymmetric Weyl semimetals, Phys. Rev. B **96**, 195119 (2017).

[62] G. Sharma, Tunable topological Nernst effect in two-dimensional transition-metal dichalcogenides, Phys. Rev. B **98**, 075416 (2018).

[63] K. Gadge, S. Tewari, and G. Sharma, Anomalous Hall and Nernst effects in Kane fermions, Phys. Rev. B **105**, 235420 (2022).

[64] D. Xiao, M.-C. Chang, and Q. Niu, Berry phase effects on electronic properties, Rev. Mod. Phys. **82**, 1959 (2010).